

## ARTICLE OPEN



# Layer-dependent Schottky contact at van der Waals interfaces: V-doped WSe<sub>2</sub> on graphene

Samuel Stolz<sup>1,2</sup>, Azimkhan Kozhakhmetov<sup>3,4</sup>, Chengye Dong<sup>4</sup>, Oliver Gröning<sup>1</sup>, Joshua A. Robinson<sup>3,4,5</sup> and Bruno Schuler<sup>1</sup>✉

Contacting two-dimensional (2D) semiconductors with van der Waals semimetals significantly reduces the contact resistance and Fermi level pinning due to defect-free interfaces. However, depending on the band alignment, a Schottky barrier remains. Here we study the evolution of the valence and conduction band edges in pristine and heavily vanadium (0.44%), i.e., *p*-type, doped epitaxial WSe<sub>2</sub> on quasi-freestanding graphene (QFEG) on silicon carbide as a function of thickness. We find that with increasing number of layers the Fermi level of the doped WSe<sub>2</sub> gets pinned at the highest dopant level for three or more monolayers. This implies a charge depletion region of about 1.6 nm. Consequently, V dopants in the first and second WSe<sub>2</sub> layer on QFEG/SiC are ionized (negatively charged) whereas they are charge neutral beyond the second layer.

*npj 2D Materials and Applications* (2022)6:66; <https://doi.org/10.1038/s41699-022-00342-4>

## INTRODUCTION

Layered two-dimensional (2D) transition metal dichalcogenide (TMDC) semiconductors are promising beyond silicon materials owing to their attractive optoelectronic properties<sup>1–4</sup> and weak inter-layer coupling that overcomes vital engineering challenges of bulk materials regarding heteromaterial integration and miniaturization. Among potential applications for 2D-TMDCs are stacked nanosheet field effect transistors,<sup>5,6</sup> lateral heterojunction diodes<sup>7–10</sup>, or photodetectors<sup>11,12</sup>, which all require high-quality 2D-TMDCs with tunable electronic properties. Hence, huge effort is devoted to establish high-quality scalable production<sup>13</sup>, controlled doping<sup>14–22</sup>, and optimized electronic contacts<sup>23–29</sup>.

In recent years, epitaxial growth of wafer-scale substitutionally doped semiconducting 2D-TMDCs such as MoS<sub>2</sub>, WS<sub>2</sub>, and WSe<sub>2</sub> has been successfully established using metalorganic chemical vapor deposition (MOCVD). Doping with nonisovalent transition metals such as V<sup>21</sup> and Nb<sup>30</sup> or Re<sup>18,31</sup> and Mn<sup>32</sup> yielded the expected *p*-type or *n*-type behavior, respectively, but it was noted that dopant ionization energies are significantly higher in the monolayer limit due to strong defect state localization<sup>33</sup>. Moreover, for metal-TMDC contacts, Fermi level pinning because of metal-induced gap states (MIGS) at the interface or due to disorder-order induced gap states, which originate from vacancies or substitutional defects, reduce the tunability of the Schottky barrier height and results in high contact resistance, thus limiting device performance<sup>24,27,28,34–37</sup>. Van der Waals semimetals like graphene or graphite greatly suppress the formation of MIGS owing to their low density of states at the Fermi level while at the same time reducing interface disorder through the absence of dangling bonds.

Here we investigate the layer-dependent valence and conduction band onsets of a prototypical semimetal–TMDC contact formed between multilayer WSe<sub>2</sub> grown on quasi-freestanding epitaxial graphene on 6H-SiC(0001) (QFEG/SiC) (Fig. 1a, b). By means of scanning tunneling microscopy and spectroscopy (STM/S) we compare the band onset evolution from 1 to 7 monolayers (ML) between *p*-type V-doped (0.44%,  $4.7 \cdot 10^{12} \text{ cm}^{-2}$ ) and nominally

undoped WSe<sub>2</sub>. For the V-doped WSe<sub>2</sub> we find that the Fermi level is pinned to the defect state energy from 3 ML on, whereas the Fermi level resides in the band gap in the mono- and bilayer case, suggesting a charge depletion region of around 1.6 nm.

## RESULTS AND DISCUSSION

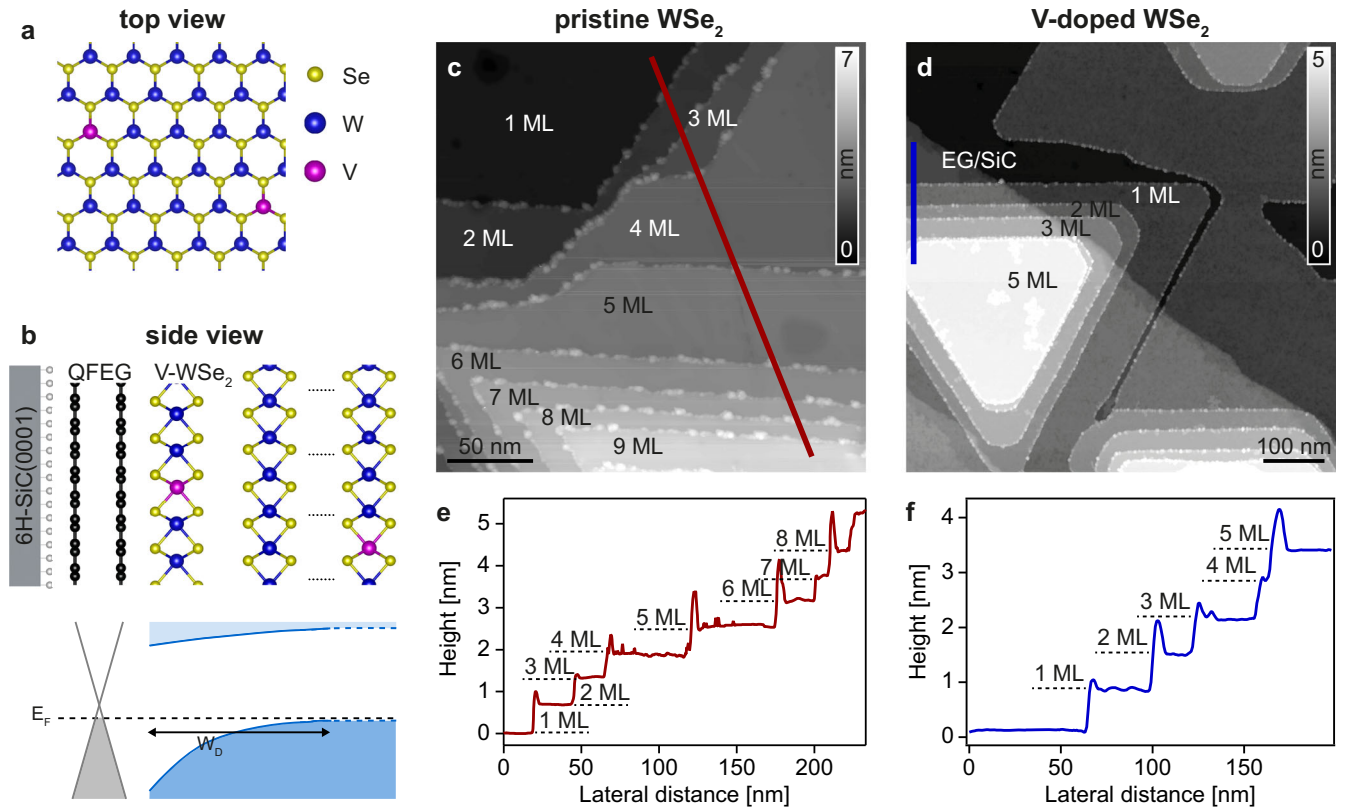
### Layer-dependent STS of undoped WSe<sub>2</sub>

Figure 1c, d show large-scale STM topography images of undoped and V-doped WSe<sub>2</sub> samples grown on QFEG/SiC. For both samples multilayer WSe<sub>2</sub> regions can be found. After identifying the QFEG and single-layered WSe<sub>2</sub> by their distinct STS fingerprints, we determine the number of WSe<sub>2</sub> ML by counting the number of discrete steps of 0.65 nm height, as depicted in the height-profiles shown in Fig. 1e, f.

Figure 2 summarizes the layer-dependent STM/STS results obtained for undoped WSe<sub>2</sub>. As exemplarily shown in the STM image of 1 ML of undoped WSe<sub>2</sub> in Fig. 2a, the dominant type of defect that we observe occurs with a density below 0.02% and is identified as molybdenum atoms that substituted W<sup>38</sup>. As depicted in Fig. 1b, the local density of states of 1 ML undoped WSe<sub>2</sub> revealed by STS exhibits distinct valence and conduction band edges with the Fermi level (at zero sample bias  $V_B$ ) close to the center of the 2.34 eV band gap. The layer dependence of the valence and conduction band edges and of the band gap for undoped WSe<sub>2</sub> is shown in Fig. 2b, c. Independent of the number of layers, the Fermi level is close to the center of the band gap for undoped WSe<sub>2</sub>. With increasing number of layers, both, the conduction and the valence band edge of undoped WSe<sub>2</sub> move symmetrically toward the Fermi energy, hence lowering the band gap for thicker films due to inter-layer hybridization. The evolution of the band gap with the number of layers is qualitatively in good agreement with previous reports<sup>39–41</sup>.

When examining the layer dependent STS data of undoped WSe<sub>2</sub> in more detail, we find that for more than 1 ML WSe<sub>2</sub> additional steps in the local density of states of the valence band

<sup>1</sup>nanotech@surfaces Laboratory, Empa—Swiss Federal Laboratories for Materials Science and Technology, Dübendorf, Switzerland. <sup>2</sup>Department of Physics, University of California, Berkeley, CA 94720, USA. <sup>3</sup>Department of Materials Science and Engineering, The Pennsylvania State University, University Park, PA 16802, USA. <sup>4</sup>Two-Dimensional Crystal Consortium, The Pennsylvania State University, University Park, PA 16802, USA. <sup>5</sup>Department of Chemistry and Department of Physics, The Pennsylvania State University, University Park, PA 16802, USA. ✉email: [bruno.schuler@empa.ch](mailto:bruno.schuler@empa.ch)



**Fig. 1** Multilayer vanadium-doped  $\text{WSe}_2$ . **a** Top view of the atomic structure of a single  $\text{WSe}_2$  layer. **b** Top: Schematic of multi-layered  $\text{WSe}_2$  grown on top of QFEG/SiC(0001) viewed from the side. Bottom: Illustration of the band alignment of multi-layered V-doped  $\text{WSe}_2$  on top of QFEG.  $W_D$  denotes the depletion depth. **c, d** Large-scale STM image ( $V_B = 1.6$  V) of multilayer undoped (**c**) and V-doped (**d**)  $\text{WSe}_2$ . The number of  $\text{WSe}_2$  layers are labelled on both images. **e, f** Height profiles of undoped (**e**) and V-doped (**f**)  $\text{WSe}_2$  taken along the lines depicted in the respective STM image. Each step in the height profile is around 0.65 nm and corresponds to a change of 1 ML.

can be seen (Fig. 2b). Such steps are indicative of a staggered DOS as expected for a 2D system<sup>42</sup>. Hence, our data suggest that every additional layer of  $\text{WSe}_2$  introduces another electron subband in the valence band spectrum. This behavior has recently also been observed in transport experiments by Takeyama et al.<sup>43</sup> and can be described by a tight binding model of weakly coupled 2D quantum wells. Thereby, the weak van der Waals inter-layer coupling is introduced by an inter-layer electron (hole) hopping term  $t_{e(h)}$ . The resulting energies of the  $n$ th subband edge is given by:  $E_{e(h)}^n = E_{e(h)} - 2t_{e(h)} \cos(\frac{n\pi}{N+1})$  where  $E_{e(h)}$  are the conduction (valence) band edges of 1 ML  $\text{WSe}_2$  and  $N$  is the number of layers<sup>44</sup>. In Fig. 2d, we plot the width of the identified energy plateaus  $E_h^n$  for 1–7 ML of undoped  $\text{WSe}_2$ . Fitting the quantum well model to the layer dependence of the valence band edge, conduction band edge, and band gap in Fig. 2c, we estimate  $E_h = -1.05 \pm 0.02$  eV,  $E_e = 1.30 \pm 0.03$  eV,  $t_h = 0.29 \pm 0.02$  eV and  $t_e = 0.21 \pm 0.02$  eV. The derived values for the hopping parameters coincide very well with those reported by Ruiz-Tijerina et al.<sup>45</sup> for  $\text{WSe}_2$  in their  $\mathbf{k} \cdot \mathbf{p}$  tight binding model theoretically investigating the intersubband transitions.

### Layer-dependent STS of vanadium-doped $\text{WSe}_2$

After having established that undoped  $\text{WSe}_2$  exhibits the expected layer-dependence, we focus on V-doped  $\text{WSe}_2$ . In Fig. 3, STM images for different numbers of layers of V-doped  $\text{WSe}_2$  are shown. When comparing the high-resolution STM images of 1 ML of undoped (Fig. 2a) and 1 ML of V-doped (Fig. 3a)  $\text{WSe}_2$  taken at positive bias voltage, we observe a high density of localized circular depressions in the STM topography for V-doped  $\text{WSe}_2$ . We identify these depressions as V dopants, because their density of about 0.44% is more than an

order of magnitude higher than the density of all impurities observed for undoped  $\text{WSe}_2$  and both, the STM and STS signatures, coincide with the one we previously reported for V atoms substituting  $\text{W}$ <sup>21</sup>. In Fig. 3b–i, the layer-dependent appearance of the V dopants is presented. At negative  $V_B$ , V dopants in the topmost layer appear as circular protrusions, independent of the number of  $\text{WSe}_2$  layers. At positive  $V_B$  on the other hand, the contrast changes from a circular (dark) depression for 1 ML and 2 ML, to a hexagonal (bright) orbital shape from 3 ML and beyond.

In Fig. 4, we analyze the layer-dependent progression of the local electronic states of the V dopants. We perform STS centered on the V dopants that are in the topmost layer of  $n$ -layered  $\text{WSe}_2$  for  $n = \{1, 2, \dots, 7\}$  and compare the results to STS of  $n$ -layered undoped and V-doped  $\text{WSe}_2$  that are recorded as far from vanadium substituents as possible given the high dopant density. The STS results for V-doped  $\text{WSe}_2$  are shown in Fig. 4a. While the band gap is also narrowing for increasing number of layers, the shift of the band edges is highly asymmetric. Whereas the conduction band onset stays roughly at the same energy, the valence band onset shifts from  $-1.18$  V (1 ML) to  $-0.12$  V (3 ML) and converges to  $\sim 0$  V for larger number of layers. On individual V dopants (Fig. 4b) we observe additional electronic states above the valence band edge as reported in Ref.<sup>21</sup> confirming their  $p$ -type character. Like the valence band maximum (VBM) of V-doped  $\text{WSe}_2$ , the localized dopant states progressively shift toward the Fermi level, where they get pinned for 3 ML and thicker samples. At the same time, the difference between the highest occupied defect state and the VBM gets smaller, indicating a weakening of the defect state binding energy. The comparison of the layer-dependent band edge evolution and band gap for V-doped  $\text{WSe}_2$  and undoped  $\text{WSe}_2$  is summarized in Fig. 4c, d.

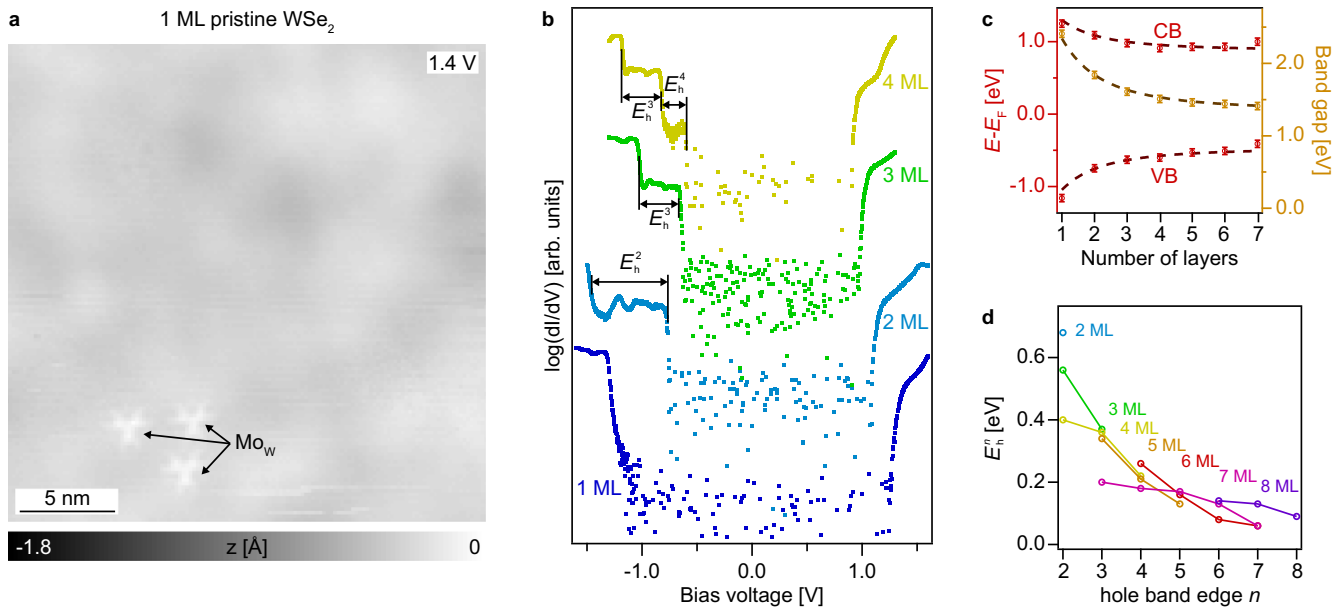


**Fig. 2** Layer-dependent electronic properties of undoped  $\text{WSe}_2$ . **a** STM image of undoped monolayer  $\text{WSe}_2$  at  $V_B = 1.4$  V. **b** Layer dependent STS signal of undoped  $\text{WSe}_2$ . **c** The experimentally determined conduction band edge, valence band edge, and band gap of undoped  $\text{WSe}_2$  as a function of layer count (markers). The experimental data in (c) is fitted with the tight binding model presented in the text (dashed lines). **d** The energy of each plateau identified in the STS of undoped  $\text{WSe}_2$  plotted versus the corresponding number of hole band edge  $n$  in the quantum well model.

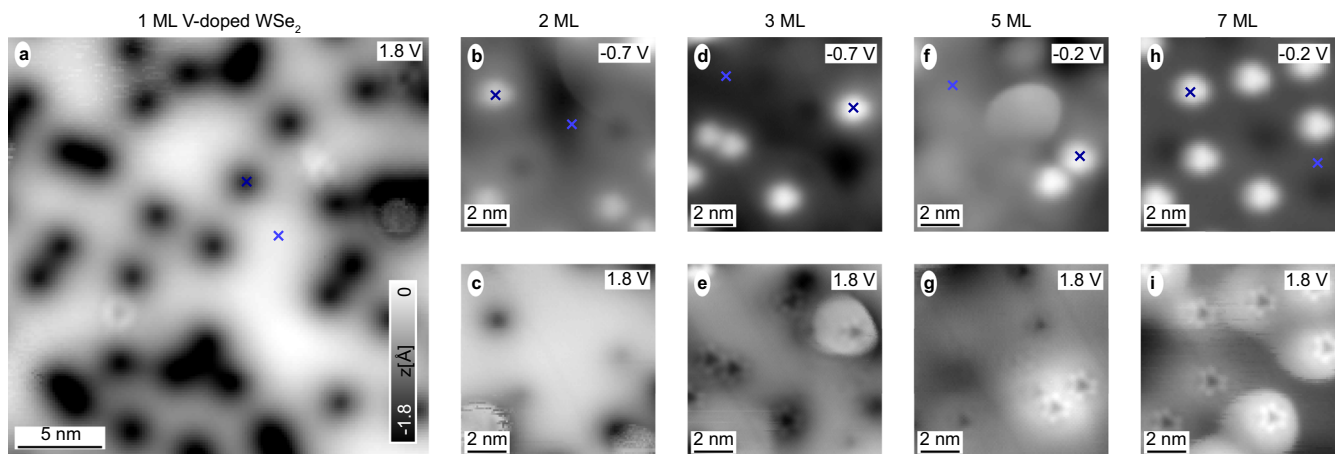


**Fig. 3** Layer-dependent appearance of vanadium dopants. **a–i** STM images of 1 ML (a), 2 ML (b, c), 3 ML (d, e), 5 ML (f, g), and 7 ML (h, i) V-doped  $\text{WSe}_2$ . The blue markers indicate the positions at which the  $dI/dV$  spectra shown in Fig. 4a, b have been recorded.  $V_B$  is indicated in the top right corner in each STM image.

### Layer-dependent Schottky contact

The pinning of the valence band edge of V-doped  $\text{WSe}_2$  can be understood as a Schottky contact where the  $p$ -type dopants in the depletion region of two ML are ionized, i.e., negatively charged. For three or more ML, the charge transition level is just below zero bias voltage, hence when scanning the charge-neutral V dopants with negative bias voltage, thus probing the electronic states below the Fermi level, they exhibit the same STM signature as the negatively charged V dopants in the first and second layer V- $\text{WSe}_2$  (Fig. 3a, b, d, f, h). However, when probing the V dopants in the third or higher V- $\text{WSe}_2$  layer they appear charge-neutral.

At the graphene/TMDC interface, the position of the Fermi level with respect to the TMDC bands is determined by the work function and is essentially the same for doped and undoped  $\text{WSe}_2$  samples. In the bulk limit, the Fermi level assumes the intrinsic value in the center of the band gap for the undoped TMDC,

whereas it gets pinned at the dopant state for the V-doped TMDC, respectively. Here we quantify over how many TMDC layers this transition is happening corresponding to the depletion depth of the Schottky contact. We find that the depletion depth for the technologically relevant 2D–3D interface of layered 0.44% V-doped  $\text{WSe}_2$  on QFEG/SiC to be between 2 ML and 3 ML, which is between 1.3 nm and 1.95 nm.

In summary, we identified a distinct layer dependence of the electronic structure of pristine and  $p$ -type V-doped  $\text{WSe}_2$  on a QFEG/SiC substrate using STM/S. For pristine  $\text{WSe}_2$ , the band gap narrows symmetrically, with the Fermi level fixed to the center of the band gap. Moreover, we find that each additional  $\text{WSe}_2$  layer introduces an extra subband in the valence band spectrum. The progression of the conduction and valence band edge for 0.44% V-doped multilayer  $\text{WSe}_2$  on the other hand exhibits a prototypical Schottky contact behavior. While for monolayer V-doped  $\text{WSe}_2$  the

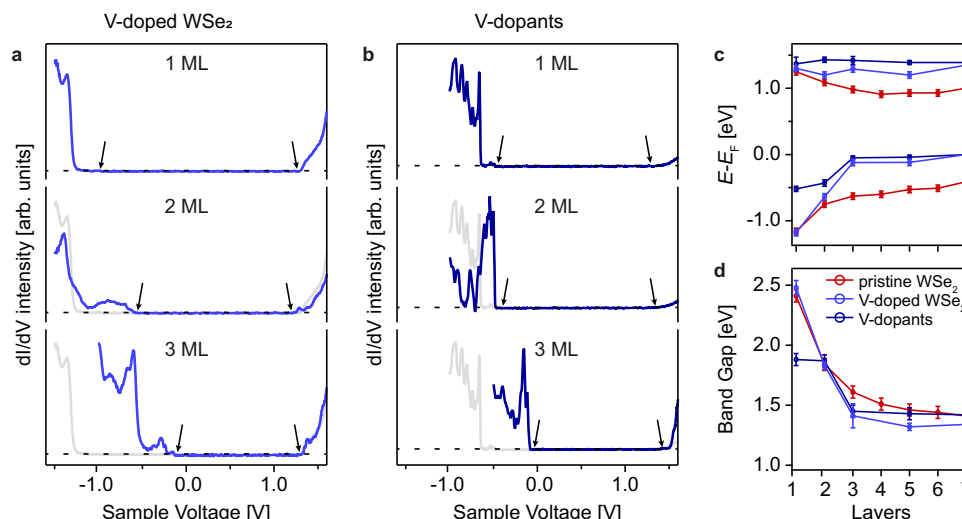


**Fig. 4** Layer-dependent electronic properties of V-doped WSe<sub>2</sub>. **a, b** STS recorded for 1–3 ML of V-doped WSe<sub>2</sub> (**a**) and of V dopants (**b**) in the topmost WSe<sub>2</sub> layer (blue). The gray lines display the 1 ML data for comparison. The black arrows indicate the positions of the valence and conduction band edges for V-doped WSe<sub>2</sub> and of the localized dopant state and the conduction band edge for V dopants. **c, d** Layer-dependence of conduction and valence band edge (**c**) and band gap (**d**) for undoped WSe<sub>2</sub> (red), V-doped WSe<sub>2</sub> (light blue), and V dopants (dark blue), respectively.

Fermi level resides close to the center of the band gap, it gets pinned to the highest dopant state upon exceeding 2 ML, corresponding to a depletion depth of about 1.6 nm.

## METHODS

### MOCVD growth of undoped and V-doped WSe<sub>2</sub> films

The undoped and V-doped WSe<sub>2</sub> samples were synthesized in a custom-designed vertical cold wall gas-source CVD reactor as reported previously in Refs. <sup>17,46</sup>. Tungsten hexacarbonyl (W(CO)<sub>6</sub>) (99.99%, Sigma-Aldrich), hydrogen selenide (H<sub>2</sub>Se) (99.99%, Matheson), and vanadium (V(C<sub>5</sub>H<sub>5</sub>)<sub>2</sub>) (sublimed, 95% Strem Chemicals) were used as metal, chalcogen, and dopant precursors, respectively, in a 100% H<sub>2</sub> ambient.

The metal and dopant precursors are kept inside stainless-steel bubblers where temperature and pressure are constantly maintained at 25 °C and 970 mbar, and 40 °C and 970 mbar, respectively. H<sub>2</sub>Se is supplied from a separate gas manifold. All three precursors are introduced from separate lines to prevent intermixing before reaching the reactor inlet. The growth of undoped and V-doped WSe<sub>2</sub> followed the three-step growth reported in Ref. <sup>47</sup>, which consists of a nucleation, a ripening, and a lateral growth stage on c-plane sapphire (Cryscore Optoelectronic LTd, 99.95%). At all three stages, the growth temperature, pressure, and H<sub>2</sub>Se flow rate were kept constantly at 800 °C, 930 mbar, and 7 sccm.

For the growth of undoped WSe<sub>2</sub>, the metal precursor is inserted with a flow rate of 20 sccm for 2 min during the nucleation phase. At the ripening stage, the W(CO)<sub>6</sub> flow is switched off and the formed nuclei are annealed in H<sub>2</sub>Se for 10 min. During the lateral growth phase, W(CO)<sub>6</sub> is re-introduced with a constant flow of 4.5 sccm.

For the growth of V-doped WSe<sub>2</sub>, V(C<sub>5</sub>H<sub>5</sub>)<sub>2</sub> was additionally inserted simultaneously with W(CO)<sub>6</sub> during the nucleation phase with a flow of 60 sccm and with a flow of 5 sccm during the lateral growth phase. The vanadium density was deduced from STM measurements.

### Scanning probe microscopy

Undoped and V-doped WSe<sub>2</sub> were prepared ex situ on QFEG on SiC substrates followed by a final 450 °C anneal in ultrahigh vacuum. The measurements were performed with a commercial

LT STM from Scienta Omicron operated at 5 K and at pressures below  $2 \cdot 10^{-10}$  mbar. The tungsten tip was prepared on a clean Au(111) surface (sputtering: 10 min, Ar<sup>+</sup>, 1 kV; annealing: 10 min, 450 °C) and confirmed to be metallic. STM topographic measurements were taken in constant current mode with the bias voltage given with respect to the sample. STS measurements were recorded using a lock-in amplifier at 860 Hz and a modulation amplitude of 10 mV. The band gap was determined as described in Ref. <sup>48</sup> by fitting the valence and conduction band edge and the band gap intensities of the logarithmic STS data with a line.

## DATA AVAILABILITY

The data that support the findings of this study are available from the corresponding author upon reasonable request.

## CODE AVAILABILITY

Upon request, authors will make available any previously unreported computer code or algorithm used to generate results that are reported in the paper and central to its main claims.

Received: 12 May 2022; Accepted: 24 August 2022;

Published online: 14 September 2022

## REFERENCES

- Kim, S. J., Choi, K., Lee, B., Kim, Y. & Hong, B. H. Materials for Flexible, Stretchable Electronics: Graphene and 2D Materials. *Annu. Rev. Mater. Res.* **45**, 63–84 (2015).
- Chhowalla, M., Jena, D. & Zhang, H. Two-dimensional semiconductors for transistors. *Nat. Rev. Mater.* **1**, 1–15 (2016).
- Manzeli, S., Ovchinnikov, D., Pasquier, D., Yazyev, O. V. & Kis, A. 2D transition metal dichalcogenides. *Nat. Rev. Mater.* **2**, 1–15 (2017).
- Kang, S. et al. 2D semiconducting materials for electronic and optoelectronic applications: potential and challenge. *2D Mater.* **7**, 022003 (2020).
- Radisavljevic, B., Radenovic, A., Brivio, J., Giacometti, V. & Kis, A. Single-layer MoS<sub>2</sub> transistors. *Nat. Nanotechnol.* **6**, 147–150 (2011).
- Sebastian, A., Pendurthi, R., Choudhury, T. H., Redwing, J. M. & Das, S. Benchmarking monolayer MoS<sub>2</sub> and WS<sub>2</sub> field-effect transistors. *Nat. Commun.* **12**, 693 (2021).
- Duan, X. et al. Lateral epitaxial growth of two-dimensional layered semiconductor heterojunctions. *Nat. Nanotechnol.* **9**, 1024–1030 (2014).
- Gong, Y. et al. Two-step growth of two-dimensional WSe<sub>2</sub>/MoS<sub>2</sub> heterostructures. *Nano Lett.* **15**, 6135–6141 (2015).

9. Sahoo, P. K., Memaran, S., Xin, Y., Balicas, L. & Gutiérrez, H. R. One-pot growth of two-dimensional lateral heterostructures via sequential edge-epitaxy. *Nature* **553**, 63–67 (2018).
10. Utama, M. I. B. et al. A dielectric-defined lateral heterojunction in a monolayer semiconductor. *Nat. Electron.* **2**, 60–65 (2019).
11. Lopez-Sanchez, O., Lembke, D., Kayci, M., Radenovic, A. & Kis, A. Ultrasensitive photodetectors based on monolayer MoS<sub>2</sub>. *Nat. Nanotechnol.* **8**, 497–501 (2013).
12. Jayachandran, D. et al. A low-power biomimetic collision detector based on an in-memory molybdenum disulfide photodetector. *Nat. Electron.* **3**, 646–655 (2020).
13. Kang, K. et al. High-mobility three-atom-thick semiconducting films with wafer-scale homogeneity. *Nature* **520**, 656–660 (2015).
14. Habib, M. et al. Ferromagnetism in CVT grown tungsten diselenide single crystals with nickel doping. *Nanotechnology* **29**, 115701 (2018).
15. Yang, L. et al. Ta Doping Enhanced Room-Temperature Ferromagnetism in 2D Semiconducting MoTe<sub>2</sub> Nanosheets. *Adv. Electron. Mater.* **5**, 1900552 (2019).
16. Chu, D. & Kim, E. K. Hole conduction of tungsten diselenide crystalline transistors by niobium dopant. *Adv. Electron. Mater.* **5**, 1800695 (2019).
17. Kozhakhmetov, A. et al. Scalable BEOL compatible 2D tungsten diselenide. *2D Mater.* **7**, 015029 (2019).
18. Kozhakhmetov, A. et al. Scalable Substitutional Re-Doping and its Impact on the Optical and Electronic Properties of Tungsten Diselenide. *Adv. Mater.* **32**, 2005159 (2020).
19. Yun, S. J. et al. Ferromagnetic Order at Room Temperature in Monolayer WSe<sub>2</sub> Semiconductor via Vanadium Dopant. *Adv. Sci.* **7**, 1903076 (2020).
20. Li, S. et al. Tunable Doping of Rhenium and Vanadium into Transition Metal Dichalcogenides for Two-Dimensional Electronics. *Adv. Sci.* **8**, 2004438 (2021).
21. Kozhakhmetov, A. et al. Controllable p-type doping of 2d WSe<sub>2</sub> via vanadium substitution. *Adv. Funct. Mater.* **31**, 2105252 (2021).
22. Lin, Y.-C., Torsi, R., Geoghegan, D. B., Robinson, J. A. & Xiao, K. Controllable Thin-Film Approaches for Doping and Alloying Transition Metal Dichalcogenides Monolayers. *Adv. Sci.* **8**, 2004249 (2021).
23. Allain, A., Kang, J., Banerjee, K. & Kis, A. Electrical contacts to two-dimensional semiconductors. *Nat. Mater.* **14**, 1195–1205 (2015).
24. Retamal, J. R. D., Periyangounder, D., Ke, J.-J., Tsai, M.-L. & He, J.-H. Charge carrier injection and transport engineering in two-dimensional transition metal dichalcogenides. *Chem. Sci.* **9**, 7727–7745 (2018).
25. Liu, Y. et al. Approaching the schottky-mott limit in van der waals metal-semiconductor junctions. *Nature* **557**, 696–700 (2018).
26. Went, C. M. et al. A new metal transfer process for van der waals contacts to vertical schottky-junction transition metal dichalcogenide photovoltaics. *Sci. Adv.* **5**, eaax6061 (2019).
27. Zhang, X. et al. Near-ideal van der Waals rectifiers based on all-two-dimensional Schottky junctions. *Nat. Commun.* **12**, 1522 (2021).
28. Park, S. et al. The Schottky-Mott rule expanded for two-dimensional semiconductors: Influence of substrate dielectric screening. *ACS Nano* **15**, 14794–14803 (2021).
29. Kwon, G. et al. Interaction- and defect-free van der waals contacts between metals and two-dimensional semiconductors. *Nat. Electron.* **5**, 241–247 (2022).
30. Zhang, K. et al. Tuning transport and chemical sensitivity via niobium doping of synthetic MoS<sub>2</sub>. *Adv. Mater. Interfac.* **7**, 2000856 (2020).
31. Zhang, K. et al. Tuning the electronic and photonic properties of monolayer mos<sub>2</sub> via in situ rhenium substitutional doping. *Adv. Funct. Mater.* **28**, 1706950 (2018).
32. Zhang, K. et al. Manganese doping of monolayer MoS<sub>2</sub>: the substrate is critical. *Nano Lett.* **15**, 6586–6591 (2015).
33. Zhu, G.-J., Xu, Y.-G., Gong, X.-G., Yang, J.-H. & Yakobson, B. I. Dimensionality-inhibited chemical doping in two-dimensional semiconductors: The phosphorene and MoS<sub>2</sub> from charge-correction method. *Nano Lett.* **21**, 6711–6717 (2021).
34. Sotthewes, K. et al. Universal fermi-level pinning in transition-metal dichalcogenides. *J. Phys. Chem. C* **123**, 5411–5420 (2019).
35. Shen, P.-C. et al. Ultralow contact resistance between semimetal and monolayer semiconductors. *Nature* **593**, 211–217 (2021).
36. Rhoads, D., Chae, S. H., Ribeiro-Palau, R. & Hone, J. Disorder in van der Waals heterostructures of 2D materials. *Nat. Mater.* **18**, 541–549 (2019).
37. Liu, X., Choi, M. S., Hwang, E., Yoo, W. J. & Sun, J. Fermi level pinning dependent 2D semiconductor devices: challenges and prospects. *Adv. Mater.* <https://doi.org/10.1002/adma.202108425> (2021).
38. Schuler, B. et al. How Substitutional Point Defects in Two-Dimensional WS<sub>2</sub> Induce Charge Localization, Spin-Orbit Splitting, and Strain. *ACS Nano* **13**, 10520–10534 (2019).
39. Prakash, A. & Appenzeller, J. Bandgap Extraction and Device Analysis of Ionic Liquid Gated WSe<sub>2</sub> Schottky Barrier Transistors. *ACS Nano* **11**, 1626–1632 (2017).
40. Nguyen, P. V. et al. Visualizing electrostatic gating effects in two-dimensional heterostructures. *Nature* **572**, 220–223 (2019).
41. Kim, H.-g. & Choi, H. J. Thickness dependence of work function, ionization energy, and electron affinity of Mo and W dichalcogenides from DFT and GW calculations. *Phys. Rev. B* **103**, 085404 (2021).
42. Kittel, C. *Introduction to solid state physics*. 8th edn (Wiley, 2005).
43. Takeyama, K. et al. Resonant tunneling due to van der waals quantum-well states of few-layers WSe<sub>2</sub> in WSe<sub>2</sub>/h-BN/p<sup>+</sup>-MoS<sub>2</sub> junction. *Nano Lett.* **21**, 3929–3934 (2021).
44. Chaves, A. et al. Bandgap engineering of two-dimensional semiconductor materials. *npj 2D Mater. Appl.* **4**, 1–21 (2020).
45. Ruiz-Tijerina, D. A., Danovich, M., Yelgel, C., Zólyomi, V. & Fal'ko, V. I. Hybrid k · p tight-binding model for subbands and infrared intersubband optics in few-layer films of transition-metal dichalcogenides: MoS<sub>2</sub>, MoSe<sub>2</sub>, WS<sub>2</sub>, and WSe<sub>2</sub>. *Phys. Rev. B* **98**, 035411 (2018).
46. Liu, B. et al. Chemical Vapor Deposition Growth of Monolayer WSe<sub>2</sub> with Tunable Device Characteristics and Growth Mechanism Study. *ACS Nano* **9**, 6119–6127 (2015).
47. Zhang, X. et al. Diffusion-Controlled Epitaxy of Large Area Coalesced WSe<sub>2</sub> Monolayers on Sapphire. *Nano Lett.* **18**, 1049–1056 (2018).
48. Tang, S. et al. Quantum spin Hall state in monolayer 1T'-WTe<sub>2</sub>. *Nat. Phys.* **13**, 683–687 (2017).

## ACKNOWLEDGEMENTS

S.S. acknowledges funding from the Swiss National Science Foundation under the project numbers 159690 and 195133. A.K. and J.A.R. acknowledge Intel through the Semiconductor Research Corporation (SRC) Task 2746 and the Penn State 2D Crystal Consortium Materials Innovation Platform (2DCC-MIP) under NSF cooperative agreement DMR-1539916 for financial support. B.S. appreciates funding from the European Research Council (ERC) under the European Union's Horizon 2020 research and innovation program (Grant agreement No. 948243).

## AUTHOR CONTRIBUTIONS

B.S. conceived the project. C.D. prepared the QFEG/SiC substrates and A.K. grew the undoped and V-doped WSe<sub>2</sub> samples, both under the supervision of J.A.R. S.S., and B.S. performed the STM experiments. S.S., B.S., and O.G. analyzed the STM experiments. S.S. and B.S. wrote the paper with inputs from all co-authors.

## COMPETING INTERESTS

The authors declare no competing interests.

## ADDITIONAL INFORMATION

**Correspondence** and requests for materials should be addressed to Bruno Schuler.

**Reprints and permission information** is available at <http://www.nature.com/reprints>

**Publisher's note** Springer Nature remains neutral with regard to jurisdictional claims in published maps and institutional affiliations.



**Open Access** This article is licensed under a Creative Commons Attribution 4.0 International License, which permits use, sharing, adaptation, distribution and reproduction in any medium or format, as long as you give appropriate credit to the original author(s) and the source, provide a link to the Creative Commons license, and indicate if changes were made. The images or other third party material in this article are included in the article's Creative Commons license, unless indicated otherwise in a credit line to the material. If material is not included in the article's Creative Commons license and your intended use is not permitted by statutory regulation or exceeds the permitted use, you will need to obtain permission directly from the copyright holder. To view a copy of this license, visit <http://creativecommons.org/licenses/by/4.0/>.

© The Author(s) 2022